arXiv:1303.1188v1 [physics.optics] 5 Mar 2013

Self-calibrating ultra-low noise, wide-bandwidth optomechanical accelerometer

Felipe Guzmán Cervantes,[1, 2, *] Lee Kumanchik,[1, 2, *] Jon Pratt,[1] and Jacob M. Taylor[1, 2, †]
[1]National Institute of Standards and Technology,
100 Bureau Drive, Gaithersburg, MD 20899, USA.
[2]Joint Quantum Institute, University of Maryland, College Park, MD 20742, USA.

The reflection spectrum of an optical cavity is exquisitely sensitive to length variations, enabling precise and accurate displacement measurements[1, 2]. When combined with mechanical oscillators, such cavities can yield accelerometers of unprecedented resolution. Previously, accelerometer sensitivity enhancements were achieved by lowering the sensor's natural frequency[3] and bandwidth. Detection near the thermal limit was achieved, but at high acceleration levels due to low oscillator mass[4]. We present a novel self-calibrating accelerometer, capable of reaching nano-$g_n/\sqrt{\mathrm{Hz}}$ sensitivities ($\mu\mathrm{Gal}/\sqrt{\mathrm{Hz}} - 1\,g_n = 9.81\,\mathrm{m/s^2}$ – equivalent displacement of $10^{-18}\,\mathrm{m}/\sqrt{\mathrm{Hz}}$) over a bandwidth of several kHz, and compare its accuracy to a calibrated commercial system. It consists of a compact ($10.6\times15\,\mathrm{mm}$), high-$mQ$ ($5\,\mathrm{kg}$) fused-silica oscillator that utilizes fiber-optic micro-mirror cavities, for self-calibrated detection of the motions of its test-mass[5]. This device provides a substantial improvement over conventional systems in accelerometry, standards and calibrations, optomechanics, seismology and gravimetry.

Accelerometer resolution is fundamentally limited by thermal fluctuations of the test-mass, which for a simple harmonic oscillator at high temperature is given by[6],

$$a_{th} = \sqrt{\frac{4k_B T\omega_o}{mQ}}, \tag{1}$$

where k_B is the Boltzmann's constant, T is temperature, ω_o is the natural frequency of the harmonic oscillator, m is the oscillator mass, and Q is the mechanical quality factor. Typically, the acceleration is inferred from a displacement measurement which has a frequency response[3, 7],

$$\frac{X(\omega)}{A(\omega)} = -\frac{1}{\omega_o^2 - \omega^2 + i\,\frac{\omega_o}{Q}\omega}, \tag{2}$$

where $X(\omega)$ is the relative displacement given an input acceleration $A(\omega)$ at an angular frequency ω. The displacement noise floor is a function of the device bandwidth by $x_{th} = a_{th}/\omega_o^2$. Performance at nano$-g_n$ has been obtained[8, 9], however, only at severely limiting bandwidths, e.g. below 100 Hz.

From Equation 2, nano$-g_n/\sqrt{\mathrm{Hz}}$-resolution over a 10 kHz bandwidth requires detection sensitivities of $10^{-18}\,\mathrm{m}/\sqrt{\mathrm{Hz}}$. Optical detection schemes such as Fabry-Pérot interferometry offer this type of resolution, with the added benefit of intrinsic accuracy, since the International System of Units (SI) defines length in terms of the wavelength of light. Thus, if test-mass motion is measured in terms of an optical cavity referenced to a physical standard such as an atomic transition, all that is required to convert $X(\omega)$ to acceleration is an estimate of ω_o, a simple frequency measurement. Current wavelength and frequency calibrations reach accuracies of 10^{-11} and 10^{-15} respectively. State-of-the-art acceleration calibrations only reach levels of 10^{-2}[10] at discrete frequency points. Moreover, it is highly challenging to conduct accurate system identification[11, 12] in conventional accelerometer systems, which strongly limits the detection bandwidth significantly below the mechanical resonance (typically $\omega_o/5$). In contrast, the displacement-to-acceleration transfer function (Equation 2) depends only on two parameters, Q and ω_o that are independently measured via a ringdown technique (see Methods), providing a complete system characterization. This associated with the self-calibrating nature of the displacement detection scheme, provides high-sensitivity measurements over a continuous frequency bandwidth of several kHz, even beyond the mechanical resonance, proving itself revolutionary.

The mechanical fused-silica oscillator is shown in Figure 1a. This material was chosen for its compatibility with fiber optics and its inherent low loss ($fQ > 10^{13}$[13] or $Q > 10^9$ at 10 kHz) characteristics. The mechanical oscillator was laser-assist micro-machined from a 2 mm thick fused-silica wafer to produce a monolithic device. The base of the oscillator was frit-bonded to a fused-silica substrate and the moving portion was suspended over a laser-machined relief. The overall design targeted a thermally-limited sensitivity of $2\,\mathrm{n}g_n/\sqrt{\mathrm{Hz}}$, while aiming for a highly compact device. This required a high Q to compensate for a lower mass, fulfilling the condition $mQ \geq 1\,\mathrm{kg}$. This is a simplified design criterion given that m, Q, and ω_o are interrelated[14]. A factor to consider is the estimation of the limiting dissipation source, which in our case was anchor loss, predicting a maximal Q of 10^6[15, 16]. The mechanical quality factor was measured to be $Q = 2 \times 10^5$, applying a ringdown technique in vacuum. The reduced quality factor can be attributed to lossy frit-bonding material used for

---

[*] These authors contributed equally to this work.
[†] Corresponding author: jacob.taylor@nist.gov

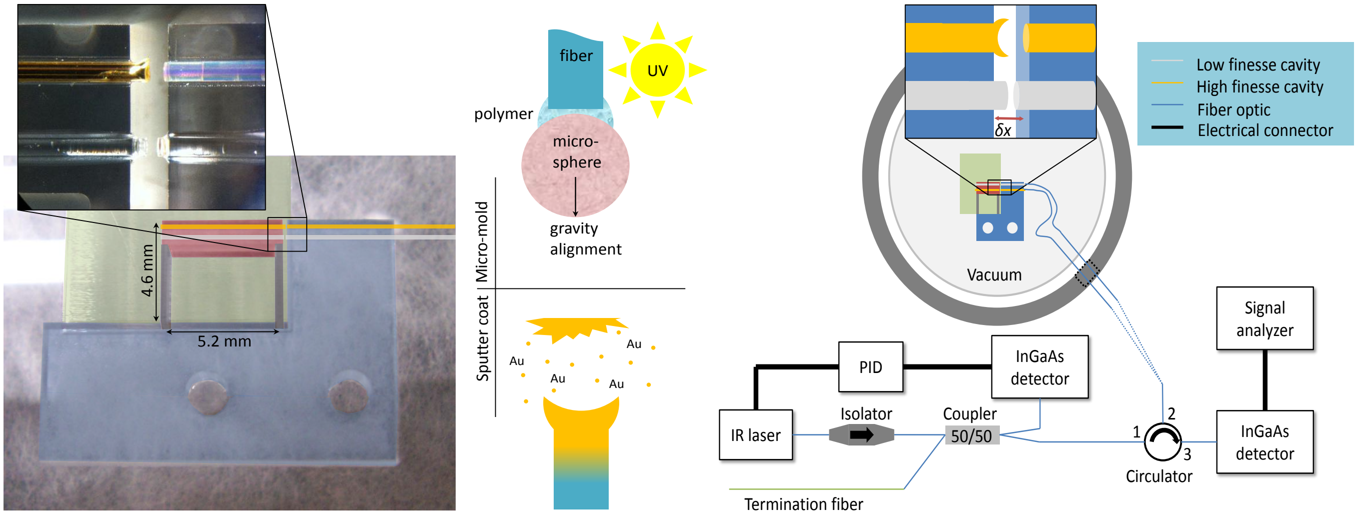

(a) (b)

FIG. 1: **Mechanical oscillator and measurement setup.** **a**, Photograph of the monolithic fused-silica mechanical oscillator with the integrated fiber micro-cavity. The fiber optic micro-cavities appear magnified on the left, the top cavity being the focus of the current discussion; the gold-coated concave fiber mirror is located in the upper left V-groove and builds a cavity with the flat, dielectrically coated fiber in the upper right V-groove. Polymer micro-molding with a 350 µm diameter ruby microsphere, and the gold coating process to manufacture the concave fiber mirror are depicted on the right. **b**, Experiment setup schematics showing the input IR-laser through a fiber-isolator and injected into a 50/50 fiber coupler. One output of the 50/50 fiber coupler is connected to a photoreceiver that gives the input signal for a PID servo feedback for laser intensity control. The other output of the 50/50 coupler is connected to a circulator that injects the light into the cavity, and launches the reflected cavity light onto the detection photoreceiver, which is connected to a spectrum analyzer for the length measurement. The sensor is located in a vacuum chamber. Fiber feed-throughs are use to transport the input and output laser beams.

mounting onto the substrate. The mass of the oscillator is 25 mg and $\omega_o = 2\pi \times 10\,800\,\mathrm{rad/s}$ yielding a net product $mQ \approx 5\,\mathrm{kg}$ and a predicted thermal noise floor of $a_{th} \approx 1.5\,\mathrm{n}g_n/\sqrt{\mathrm{Hz}}$ at room temperature.

A fiber-based micro-mirror Fabry-Pérot cavity was set up in reflection as the optical readout. The sensor ground platform and the moving mass were equipped with collinear V-grooves as alignment canals for the fiber-based mirrors. The shot-noise limited performance of the cavity length measurement is given by[1],

$$x_{SN} = \frac{1}{8\mathcal{F}}\sqrt{\frac{hc\lambda}{P}}, \tag{3}$$

where h is Planck's constant, c is the speed of light, λ is the laser wavelength, P is the laser optical output power, $\mathcal{F}$ is the cavity finesse, and x_{SN} is in units of $\mathrm{m}/\sqrt{\mathrm{Hz}}$. Thermally limited acceleration sensitivity levels of $1.5\,\mathrm{n}g_n/\sqrt{\mathrm{Hz}}$ require an equivalent shot-noise limited displacement sensitivity of $3 \times 10^{-18}\,\mathrm{m}/\sqrt{\mathrm{Hz}}$.

We utilized a telecom laser at a nominal wavelength of $\lambda = 1550\,\mathrm{nm}$ with moderate power of approximately 1 mW. Shot-noise limited sensitivity requires a cavity Finesse of about 10^3. These Finesse levels require high reflectivity mirrors, preferably with dielectric coatings, and refocusing optics at the fiber ends to obtain stable cavity modes[17]. We opted for a preliminary approach of building a plane-concave fiber-optic cavity. The input mirror consists of a perpendicularly cleaved, dielectrically coated (95%) fiber. The cavity end mirror consists of a fiber with a polymer-based micro-molded gold-coated concave mirror (see Methods). Gold typically exhibits a reflectivity of 97%, however, the net reflectivity of the cavity will be dominated by the least reflective surface, which is the input fiber mirror. The resulting cavity Finesse was measured to be approximately 60, meaning that we were limited by the optical readout sensitivity. Nevertheless, a clear path forward to thermally-limited acceleration sensitivity lies on improving the cavity Finesse by, for example, utilizing high reflectivity coatings[18].

The optical output of the Fabry-Pérot cavity in reflection is a function of the laser wavelength λ, yielding a signal $V(\lambda)$ (see Figure 2) at the photoreceiver given by,

$$V(\lambda) = A\left(1 - \gamma\frac{1}{1 + \left(\sin^2\left(\frac{\pi}{2\mathcal{F}}\right)\right)^{-1}\sin^2\left(\frac{2\pi L}{\lambda}\right)}\right)\ [\mathrm{V}], \tag{4}$$

where A is the amplitude of the signal, γ is the visibility of the cavity, L is the optical cavity length, and $\mathcal{F}$ is the cavity Finesse. Given the wide tunability range of our laser, it is possible to measure the Free Spectral Range (FSR) of the cavity and directly measure the optical cavity length L as,

$$L = \frac{c}{2\,\mathrm{FSR}}, \tag{5}$$

which amounts to 142 µm.

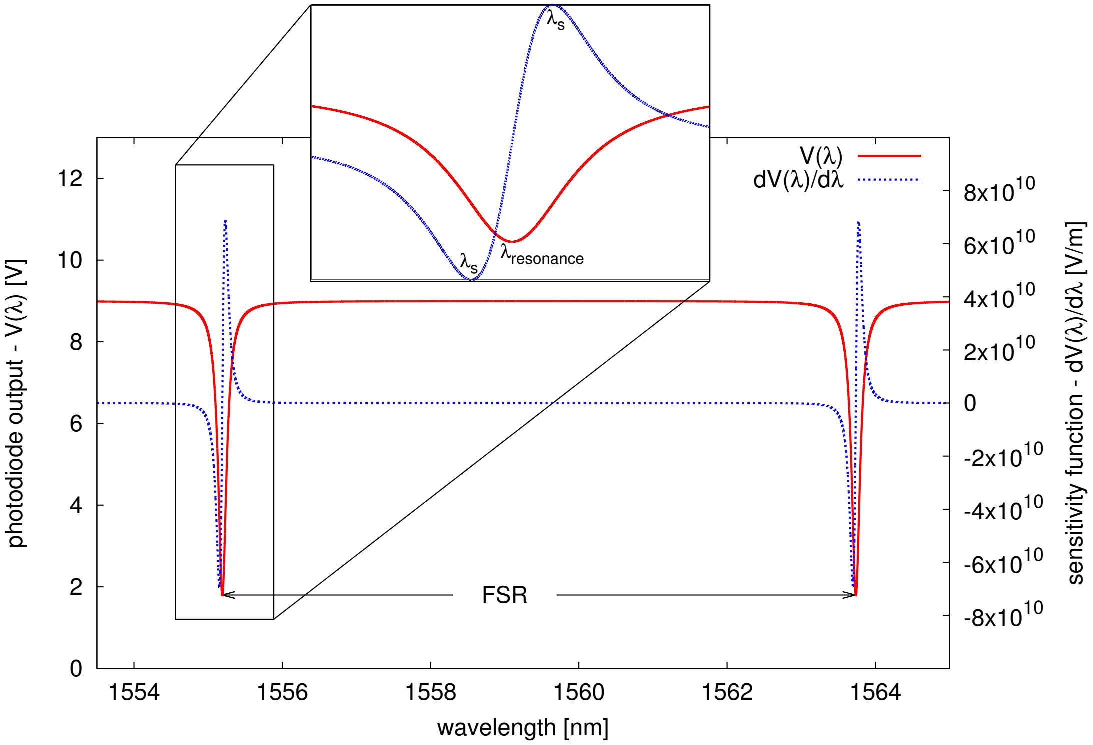

FIG. 2: **Cavity free spectral range and sensitivity.** We use a tunable laser system that can be used to measure the full free spectral range which is shown in red. The operating points of highest sensitivity are given by the maxima and minima peaks of the sensitivity function $\mathrm{d}V(\lambda)/\mathrm{d}\lambda$, plotted on the dotted blue trace. The sensitivity function $\mathrm{d}V(\lambda)/\mathrm{d}\lambda$ reaches its maximum at the two wavelength locations λ_s, symmetrically and slightly offset from the resonance wavelength $\lambda_{\mathrm{resonance}}$.

In a conventional DC readout scheme, the highest sensitivity of the cavity can be achieved by tuning the laser wavelength to the points λ_s where $|\mathrm{d}V(\lambda)/\mathrm{d}\lambda|$, obtained from the FSR measurement, reaches its maximum value (see Figure 2). Cavity length fluctuations $\mathrm{d}L$ translate to laser frequency fluctuations $\mathrm{d}\nu$ in a resonant cavity as

$$\frac{\mathrm{d}L}{L} = \frac{\mathrm{d}\nu}{\nu}, \tag{6}$$

where $\nu = c/\lambda$ is the laser frequency. Displacement fluctuations $\mathrm{d}L$ clearly couple as changes of the cavity length, thus dynamically changing the FSR. However, this effect can be neglected given that $dL \ll L$, which is approximately 12 orders of magnitude smaller in the high sensitivity measurements we present here. By combining Equations 4 and 6, it yields that measured voltage fluctuations $\mathrm{d}V$ translate as cavity length fluctuations,

$$\mathrm{d}L = \frac{L}{\lambda_s}\left(\left.\frac{\mathrm{d}V(\lambda)}{\mathrm{d}\lambda}\right|_{\lambda_s}\right)^{-1}\mathrm{d}V, \tag{7}$$

where the operating laser wavelength for maximum sensitivity λ_s is an SI-traceable quantity.

Given the self-calibrating nature of the displacement measurement and the accurate length-to-acceleration transfer function identification, the conversion to acceleration from the measured voltage is straightforward from Equations 2 and 7, and given by

$$a_n = \left|\left|\omega_o^2 - \omega^2 + i\,\frac{\omega_o}{Q}\omega\right|\right|\frac{L}{\lambda_s}\left(\left.\frac{\mathrm{d}V(\lambda)}{\mathrm{d}\lambda}\right|_{\lambda_s}\right)^{-1}\mathrm{d}V, \tag{8}$$

where all parameters $(Q, \omega_o, \lambda_s, \mathrm{d}V(\lambda)/\mathrm{d}\lambda|_{\lambda_s}, L)$ are easily measured and are stable.

Figure 3a illustrates the linear spectral density of two data sets of the measured displacement fluctuations and corresponding equivalent acceleration noise (Figure 3b), reaching a sensitivity level of $400\,\mathrm{am}/\sqrt{\mathrm{Hz}}$ and $200\,\mathrm{n}g_n/\sqrt{\mathrm{Hz}}$ below the mechanical resonance, respectively. Provided the capability to conduct a complete system identification over the entire observation bandwidth, the dynamic response peak acts as a mechanical amplification factor, resulting in a sensitivity enhancement that allows us to reach a nearly thermally-limited acceleration sensitivity at the $\mathrm{n}g_n/\sqrt{\mathrm{Hz}}$ level about the mechanical resonance.

Each data set consists of two traces. The first set corresponds to measurements conducted at free-running laser power shown in blue and magenta. The blue traces are where the laser was tuned to maximum sensitivity for cavity length fluctuations to measure the test-mass displacement and corresponding acceleration. The magenta trace is where the laser was detuned from the cavity resonance, operating the cavity as a mirror, only measuring

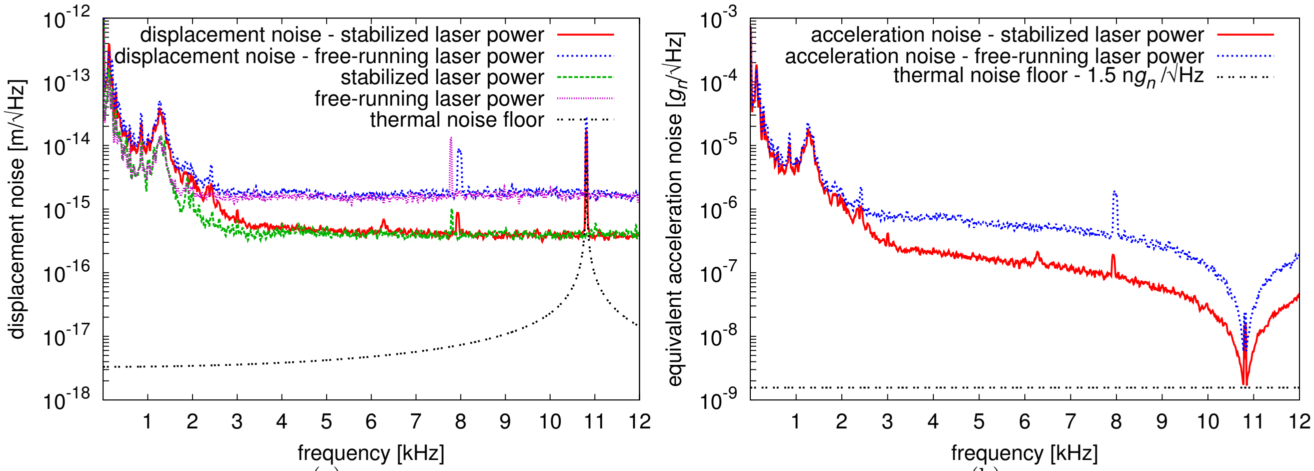

(a) (b)

FIG. 3: **Oscillator sensitivity spectra.** **a**, Linear spectral densities showing the sensitivity of the length measurement and the current limiting noise source. The dotted blue trace shows the initial sensitivity of the optical Fabry-Pérot readout while the laser power operates in a free-running condition. The dotted magenta trace outlines the equivalent displacement fluctuations of pure free-running laser intensity noise, when the laser wavelength was detuned from resonance and high-sensitivity operating points λ_s. The solid red trace depicts the length sensitivity obtained around $4 \times 10^{-16}\mathrm{m}/\sqrt{\mathrm{Hz}}$, while actively stabilizing the laser intensity through PID servo feedback. The dashed green trace shows the equivalent length fluctuations corresponding to the stabilized laser intensity. The dotted black trace shows the equivalent displacement sensitivity due to thermal noise of the mechanical oscillator, taking as input acceleration a_{th} in Equation 1 and converting it to length by the transfer function given by Equation 2. **b**, Corresponding acceleration sensitivity plots computed from the measured data plotted in **a** by using the transfer function in Equation 2.

the noise contribution of laser power fluctuations. The second data set in Figure 3, traces in red and green, shows the same data while stabilizing the laser power using a PID control system. Our current laser system only offers an AC-coupled actuation interface which prevents significant improvement at lower frequencies. The blue and red traces (tuned wavelength to max. sensitivity) show a sharp peak above 10 kHz corresponding to the natural frequency of our device. This is a clear indication that we are sensitive to the dynamics of the device which is being thermally driven. This mechanical resonance does not appear in the green and magenta traces (detuned wavelength), which correspond to pure laser power fluctuations that can be identified as our current limiting noise source. The peaks around 8 kHz correspond to artifacts of the laser system, and the low frequency structure below 3 kHz arise from the laser and fiber-optics systematics (see Methods: Optical detection scheme).

An additional experiment was run to demonstrate the self-calibrating nature of our device. A small piezo-driven shaking platform was used to exert a controlled acceleration. For comparison, we used a 400 Hz commercial Wilcoxon 731A/P31 piezoelectric accelerometer[19] that reports a gain of 1 at 10 Hz. The acceleration measurement was performed on one device at a time, mounted on our shaker. Figure 4 shows the obtained equivalent acceleration spectral density. The acceleration peaks measured by both devices come to excellent agreement. The slight discrepancy (see Figure 4b) in amplitude of approximately 6% can be attributed to differences between the devices in mounting to the shaker table, and moment of inertia.

Not all applications require large bandwidth acceleration measurements and, therefore, design trade-offs can be considered for sensitivity enhancements significantly below the n$g_n/\sqrt{\mathrm{Hz}}$ level at expense of lower bandwidth. The simplicity, compactness and high-sensitivity performance over a wide bandwidth accompanied by advanced laser-interferometric detection highlight the novelty of this type of accelerometer for a wide variety of applications in opto-mechanics and quantum-limited light-matter interactions, absolute and reference accelerometry, including seismology, ground and space-based gravity gradiometry.

Methods

Sensor manufacturing and cavity assembly. The fused silica oscillators were glass micro-machined by laser-assisted etching[20] from fused silica wafers. This includes collinear V-grooves for fiber cavity alignment. The accelerometers were glass-frit bonded to a fused silica substrate that had a pre-machined relief, above which the moving mass would hang. The fiber optic cables were bonded to the v-grooves by UV-curing epoxy. The substrate was placed on a passive vibration isolation platform located in a vacuum chamber. The fiber optic cables were fed into the vacuum chamber through deformable capillaries that clamped circumferentially

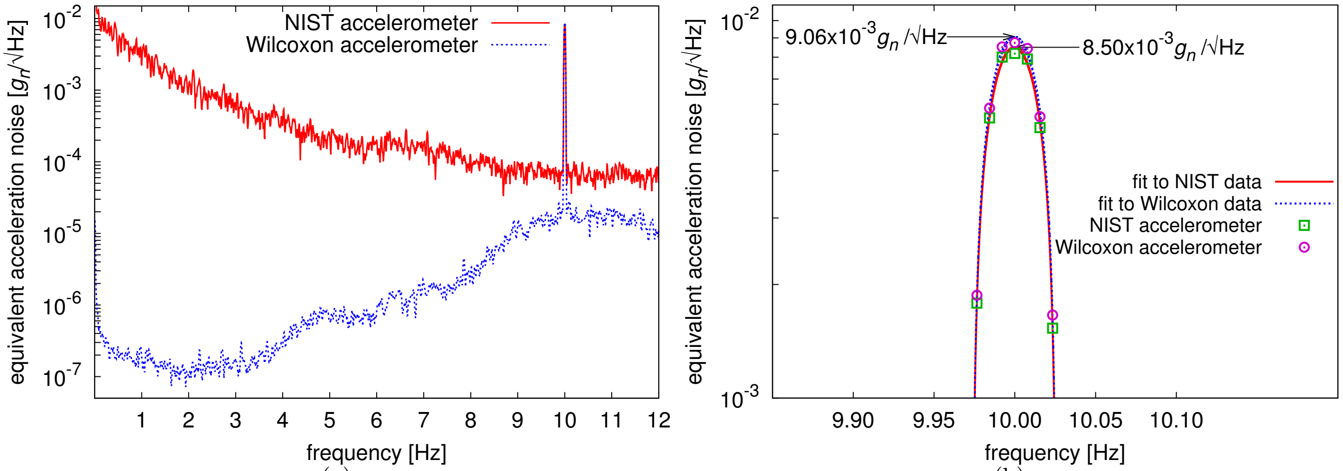

(a) (b)

FIG. 4: **Demonstration of self-calibration.** **a**, Acceleration measurement by injecting a 10 Hz signal to a piezo-driven shaker, and sensing the resulting acceleration with our device (NIST), shown by the solid red trace, and a calibrated commercial Wilcoxon accelerometer – dotted blue trace. **b**, Magnification of the measured acceleration peaks around 10 Hz, indicating the slight discrepancy in amplitude between the NIST accelerometer, in squares, and the Wilcoxon accelerometer in circles. A quadratic fit to the acceleration injection peak was computed in order to estimate the corresponding peak heights for each measurement. The error bars are given in frequency (horizontal axis) by the frequency resolution of the spectrum analyzer data, and in amplitude (vertical axis) by the spectrum analyzer noise, which is several orders of magnitude below the signal level.

around the cables for an air-tight seal. The fiber optic cables were fusion spliced to the fiber interferometer and laser sources to create a continuous strand of cable.

Optical detection scheme. Optical readout was performed by directing the back-reflected light from the cavity to a photodetector. As depicted in Figure 1b, an optical circulator was used to direct the light. Once the fiber optics are adhered to the sensor, the nominal cavity length is not adjustable. We used a highly tunable telecom laser to measure the full free-spectral range of the cavity and syntonize the laser wavelength to high-sensitivity operating points within the cavity. This setup is susceptible to parasitic cavities due to multiple reflections originating at the fiber splices and fiber ends, which result in excess intensity fluctuations arising from the unstable optical path of these parasitic interferometers.

Ring down technique for mechanical quality factor measurements. We used a piezo-shaker to excite the oscillator at resonance and measured the decay response. Resonance was determined by spectral analysis and then honed in by a high resolution function generator driving the piezo-shaker. After discontinuation of shaking, AC voltage output of the cavity photoreceiver was read out from a digital voltmeter which provided the envelope of the ring down directly. The quality factor was determined by an exponential fit to the envelope and compared to spectral analysis using the full width at half maximum (FWHM) with good agreement. Ring down is orders of magnitude faster to acquire than a high resolution spectrum minimizing the effect of frequency drift and enabling multiple trials.

Concave fiber mirror micro-molding. A photoreactive polymer was applied to the fiber tip while in a liquid state, as shown in Figure 1a. The tip was then pressed onto a Grade 25 ruby micro-sphere which clung to the polymer droplet from surface tension. Gravity was used to align the droplet and sphere to the fiber axis before curing with UV light. Once the sphere was removed, the mirror was gold-coated in-house.

---

[1] Black E. An introduction to Pound-Drever-Hall laser frequency stabilization. Am. J. Phys. 69, 79-87 (2001).
[2] Durand, M., Lawall, J. & Wang, Y. High-accuracy Fabry-Perot displacement interferometry using fiber lasers. Meas. Sci. Technol. 22, 094025 (2011).
[3] McConnell, K. & Varoto, P. Vibration Testing Theory and Practice (Wiley-Interscience, John Wiley & Sons, New York (2008).
[4] Krause, A.G., Winger, M., Blasius, T.D., Lin, Q. & Painter, O. A high-resolution microchip optomechanical accelerometer. Nat. Photon. 6, 768-772 (2012).
[5] Smith, D., Pratt, J.R. & Howard, L.P. A fiber-optic inter-

ferometer with subpicometer resolution for dc and low-frequency displacement measurement. Rev. Sci. Instrum. 80, 035105 (2009).

[6] Yasumura, K. et al. Quality Factors in Micron- and Submicron-Thick Cantilevers. J. Microelectromech. S. 9, 117-125 (2000).

[7] Braginsky, V., Khalili, F. & Thorne, K. Quantum Measurement, Cambridge University Press, (1992).

[8] Czaplewski, D. et al. Integrated NEMS and Optoelectronics for Sensor Applications. Sandia Report, SAND2007-7377 (Printed 01/2008).

[9] Krishnamoorthy, U. et al. In-plane MEMS-based nano-g accelerometer with sub-wavelength optical resonator sensor. Sensor Actuat. A-Phys. 145-146, 283-290 (2008).

[10] Payne, B.F. & Serbyn, M.R. An Application of Parameter Estimation Theory in Low Frequency Accelerometers. 14^{th} Transducer Workshop, Telemetry Group (1987).

[11] Link, A. & von Martens, H.-J. Accelerometer identification using shock excitation. Measurement 35, 191–199 (2004).

[12] Bruns, T., Link, A., Schmähling, F., Nicklich, H. & Elster, C. Calibration of accelerometers using parameter identification - Targeting a versatile new standard. XIX IMEKO World Congress, Fundamental and Applied Metrology (2009).

[13] Tabrizian, R., Rais-Zadeh, M. & Ayazi, F. Effect of phonon interactions on limiting the f.Q product of micromechanical resonators. IEEE Transducers, 2131-2134 (2009).

[14] Weinberg, M. et al. Energy loss in MEMS resonators and the impact on inertial and RF devices. IEEE Transducers, 688-695 (2009).

[15] Hao, Z. & Xu, Y. Vibration displacement on substrate due to time-harmonic stress sources from a micromechanical resonator. J. Sound Vibrat. 322, 196-215 (2009).

[16] Hao, Z., Erbil, A. & Ayazi, F. An analytical model for support loss in micromachined beam resonators with inplane flexural vibrations. Sensor Actuat. A-Phys. 109, 156-164 (2003).

[17] Hodgson, N. & Weber, H. Optical resonators: fundamentals, advanced concepts, applications. Springer Science & Business Media, Inc., New York (2005).

[18] Hunger, D., Steinmetz T., Colombe, Y., Deutsch, C., Hänsch T.W. & Reichel, J. A fiber Fabry-Perot cavity with high finesse. New J. Phys. 12, 065038(23pp) (2010).

[19] Certain commercial equipment, instruments, or materials are identified in this paper in order to specify the experimental procedure adequately. Such identification is not intended to imply recommendation or endorsement by the National Institute of Standards and Technology, nor is it intended to imply that the materials or equipment identified are necessarily the best available for the purpose.

[20] Bado, P., Said, A.A., Dugan, M. & Bellouard, Y. Laser-based fabrication of a displacement sensor with an integrated high-accuracy position sensor. SPIE Photonics West, San Jose, CA, Jan. 21-26 (2006).

Acknowledgements

We thank C. Caves, N. Malalvala, K. Lehnert, G. Shaw and E. Polzik for helpful discussions. This work was supported by the NSF Physics Frontier Center at the JQI and DARPA QuASaR and the ARO under W911NF-11-1-0212.

Author contributions

Experiment set-up, measurements, and data analysis conducted by F.G. and L.K.; data interpretation by F.G., L.K. and J.P.; experimental conception by J.P.; background and theory by J.T.; coordination provided by J.P. and J.T.; and manuscript preparation by all authors.

Competing financial interests

The authors declare no competing financial interests.